Chapter 3

Crystal Structures of $CH_3NH_3PbI_3$ and Related Perovskite Compounds Used for Solar Cells

Takeo Oku

Additional information is available at the end of the chapter

http://dx.doi.org/10.5772/59284

1. Introduction

Recently, organic-inorganic hybrid solar cells with perovskite-type pigments have been widely fabricated and rapidly studied [12, 8, 11]. Solar cells with a perovskite structure have high conversion efficiencies and stability as the organic solar cells. Since a photoconversion efficiency of 15% was achieved [2], higher efficiencies have been reported for various device structures and processes [13, 23], and the photoconversion efficiency was increased up to 19.3% [27]. The photovoltaic properties of solar cells are strongly dependent on the fabrication process, hole transport layers, electron transport layers, nanoporous layers, interfacial microstructures, and crystal structures of the perovskite compounds. Especially, the crystal structures of the perovskite-type compounds, strongly affect the electronic structures such as energy band gaps and carrier transport, and a detailed analysis of them is mandatory.

In the present article, crystal structures of perovskite-type compounds such as $CH_3NH_3PbI_3$ $CH_3NH_3PbCl_3$, $CH_3NH_3PbBr_3$, $CsSnI_3$, $CH_3NH_3GeCl_3$, and $CH_3NH_3SnCl_3$, are expected for solar cell materials, are reviewed and summarized. Since these perovskite-type materials often have nanostructures in the solar cell devices, summarized information on the crystal structures would be useful for structure analysis on the perovskite-type crystals. The nanostructures of the solar cell devices are often analysed by using X-ray diffraction (XRD) and transmission electron microscopy (TEM), and the diffraction conditions are investigated and summarized. Transmission electron microscopy, electron diffraction, and high-resolution electron microscopy are powerful tools for structure analysis of solar cells [18] and perovskite-type structures in atomic scale [17, 19].

2. Synthesis of methylammonium trihalogenoplumbates (II)

There are various fabrication processes for the methylammonium trihalogenoplumbates (II) ($CH_3NH_3PbI_3$) compound with the perovskite structures. Two typical synthesis methods for the $CH_3NH_3PbI_3$ ($MAPbI_3$) were reported [1]. $MAPbI_3$ could be synthesised from an equimolar mixture of CH_3NH_3I and PbI_2 using the reported method [8]. CH_3NH_3I was synthesised at first by reacting a concentrated aqueous solution of hydroiodic acid with methylamine, and the cleaned precipitant was mixed with PbI_2 in gamma-butyrolactone to obtain the $MAPbI_3$ product. Crystalline $MAPbI_3$ was obtained by drop-casting the solutions on glass substrates, and annealed at 100 °C. Polycrystalline $MAPbI_3$ could be also prepared by precipitation from a hydroiodic acid solution [22]. Lead(II) acetate was dissolved in a concentrated aqueous HI and heated. An HI solution with CH_3NH_2 was added to the solution, and black precipitates were formed upon cooling from 100 °C.

A typical fabrication process of the $TiO_2/CH_3NH_3PbI_3$ photovoltaic devices is also described here [28]. The details of the fabrication process is described in the reported paper [2] except for the mesoporous TiO_2 layer [16]. The photovoltaic cells were fabricated by the following process. F-Doped tin oxide (FTO) substrates were cleaned using an ultrasonic bath with acetone and methanol and dried under nitrogen gas. The 0.30M TiO_x precursor solution was prepared from titanium diisopropoxide bis(acetyl acetonate) (0.11 mL) with 1-butanol (1 mL), and the TiO_x precursor solution was spin-coated on the FTO substrate at 3000 rpm for 30 s and annealed 125 °C for 5 min. This process was performed two times, and the FTO substrate was sintered at 500 °C for 30min to form the compact TiO_2 layer. After that, mesoporous TiO_2 paste was coated on the substrate by a spin-coating method at 5000 rpm for 30 s. For the mesoporous TiO_2 layer, the TiO_2 paste was prepared with TiO_2 powder (Aerosil, P-25) with poly(ethylene glycol) in ultrapure water. The solution was mixed with acetylacetone and triton X-100 for 30min. The cells were annealed at 120 °C for 5min and at 500 °C for 30min. For the preparation of pigment with a perovskite structure, a solution of CH_3NH_3I and PbI_2 with a mole ratio of 1:1 in γ-butyrolactone (0.5 mL) was mixed at 60 °C. The solution of CH_3NH_3I and PbI_2 was then introduced into the TiO_2 mesopores by spin-coating method and annealed at 100 °C for 15min. Then, the hole transport layer (HTL) was prepared by spin coating. As the HTLs, a solution of spiro-OMeTAD (36.1 mg) in chlorobenzene (0.5 mL) was mixed with a solution of lithium bis(trifluoromethylsulfonyl) imide (Li-TFSI) in acetonitrile (0.5 mL) for 12 h. The former solution with 4-tert-butylpyridine (14.4 μL) was mixed with the Li-TFSI solution (8.8 μL) for 30min at 70 °C. Finally, gold (Au) metal contacts were evaporated as top electrodes. Layered structures of the photovoltaic cells were denoted as $FTO/TiO_2/CH_3NH_3PbI_3/HTL/Au$.

3. Crystal structures of $CH_3NH_3PbX_3$ (X=Cl, Br, or I) compounds

The crystals of methylammonium trihalogenoplumbates(II) ($CH_3NH_3PbX_3$, X=Cl, Br, or I) have perovskite structures and provide structural transitionsupon heating [24], 22]. The crystal

http://dx.doi.org/10.5772/59284

systems and transition temperatures are summarized in Table 1, as reported in the previous works [22, 21]. Atomic sites were indicated from the space group table [6]. Although the $CH_3NH_3PbX_3$ perovskite crystals have a cubic symmetry for the highest temperature phase, the CH_3NH_3 ion is polar and has C_{3v} symmetry, which should result in disordered cubic phase [14]. In addition to the disordering of the CH_3NH_3 ion, the halogen ions were also disordered in the cubic phase, as shown in Figure 1(a) and Table 2 [14]. Site occupancies were set as 1/4 for I and 1/12 for C and N. The CH_3NH_3 ion occupies 12 equivalent orientations of the C_2 axis, and hydrogen atoms have two kinds of configurations on the C_2 axis. Then, the total degree of freedom is 24 [21].

As the temperature decreases, the cubic phase is transformed in the tetragonal phase, as shown in Figure 1(b) and Table 3 [10]. The isotropic displacement parameters B were calculated as $8\pi^2 U_{iso}$. For the tetragonal phase, I ions are ordered, which resulted in the lower symmetry from the cubic phase. Site occupancies were set as 1/4 for C and N for the tetragonal $CH_3NH_3PbI_3$. As the temperature decreases lower, the tetragonal phase is transformed in the orthorhombic systems, which is due to the ordering of CH_3NH_3 ions in the unit cell, as shown in Figure 1(c) and Table 4 [1].

Energy gaps of the $CH_3NH_3PbI_3$ were also measured and calculated [1], as summrized in Table 5. The energy gap increases with increasing temperature from the *ab-initio* calculation, and the measured energy gap of ~1.5 eV is suitable for solar cell materials.

Material	**$CH_3NH_3PbCl_3$**	**$CH_3NH_3PbBr_3$**	**$CH_3NH_3PbI_3$**
Crystal system	Cubic	Cubic	Cubic
Transition temperature (K)	177	236	330
Crystal system	Tetragonal	Tetragonal	Tetragonal
Transition temperature (K)	172	149~154	161
Crystal system	Orthorhombic	Orthorhombic	Orthorhombic

Table 1. Crystal systems and transition temperatures of $CH_3NH_3PbX_3$ (X=Cl, Br, or I).

Atom	**site**	***x***	***y***	***z***	***B* (Å²)**
Pb	1*a*	0	0	0	3.32
I	12*h*	0	0.0435	0.5	8.68
N	12*j*	0.413	0.413	0.5	5.82
C	12*j*	0.578	0.578	0.5	7.05

Table 2. Structural parameters of cubic $CH_3NH_3PbI_3$. Space group *Pmm* (Z=1), *a*=6.391 Å at 330 K. B is isotropic displacement parameter.

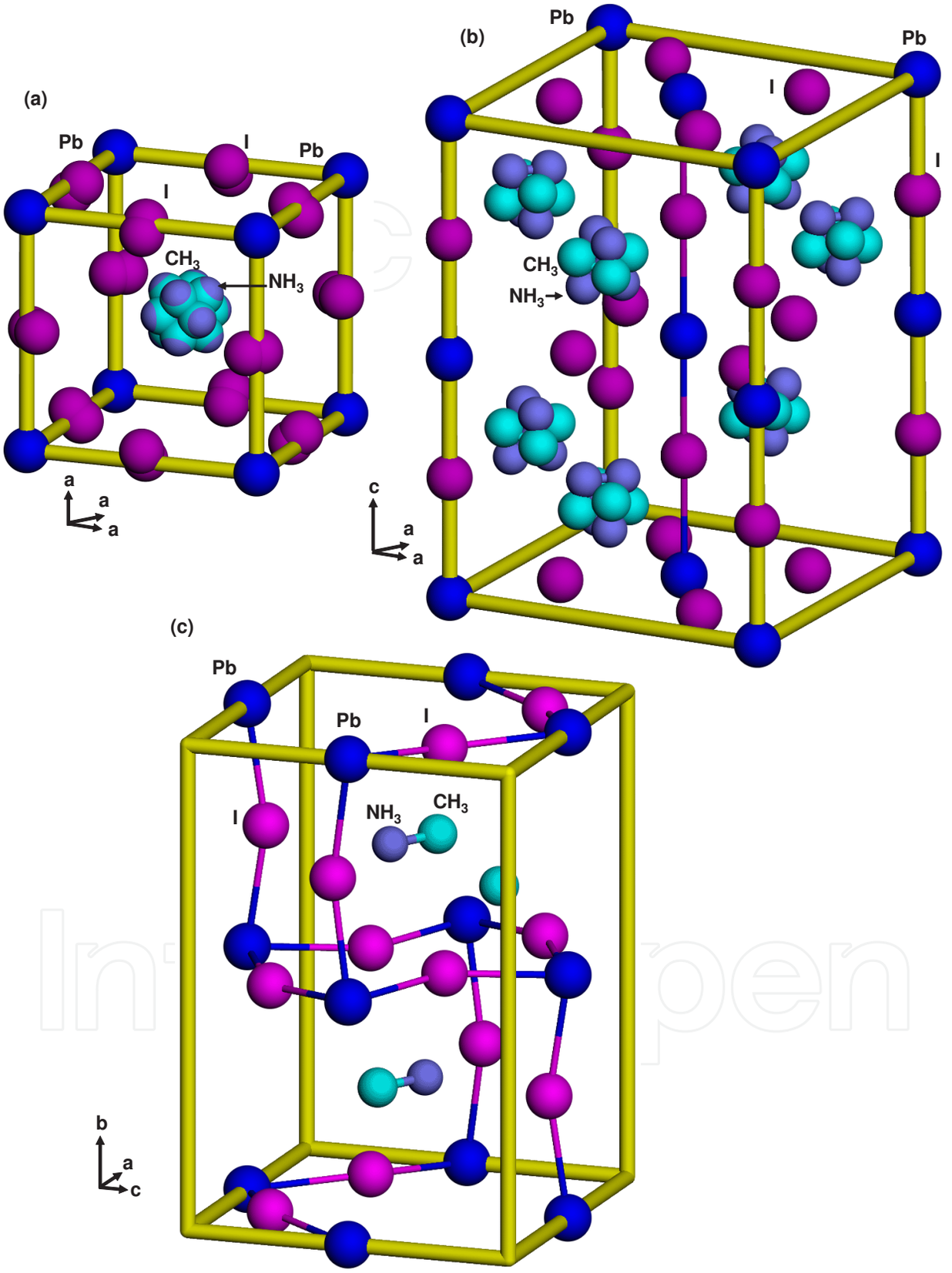

Figure 1. Structure models of $CH_3NH_3PbI_3$ with (a) cubic, (b) tetragonal and (c) orthorhombic structures.

http://dx.doi.org/10.5772/59284

Atom	site	*x*	*y*	*z*	*B* (Å²)
Pb	4*c*	0	0	0	1.63
I(1)	8*h*	0.2039	0.2961	0	4.38
I(2)	4*a*	0	0	0.25	4.11
N	16*l*	0.459	0.041	0.202	4.60
C	16*l*	0.555	–0.055	0.264	3.19

Table 3. Structural parameters of tetragonal $CH_3NH_3PbI_3$ at 220 K. Space group *I4/mcm* (Z=4), *a*=8.800 Å, *c*=12.685 Å. *B* is isotropic displacement parameter.

Atom	site	*x*	*y*	*z*	*B* (Å²)
Pb	4*b*	0.5	0	0	4.80
I(1)	4*c*	0.48572	0.25	–0.05291	1.03
I(2)	8*d*	0.19020	0.01719	0.18615	1.33
N	4*c*	0.932	0.75	0.029	2.37
C	4*c*	0.913	0.25	0.061	1.50

Table 4. Structural parameters of orthorhombic $CH_3NH_3PbI_3$ at 100 K. Space group *Pnma* (Z=4), *a*=8.8362 Å, *b*=12.5804 Å, *c*=8.5551 Å. All occupancy factors 1.0. B is isotropic displacement parameter.

Material	$CH_3NH_3PbI_3$	$CH_3NH_3PbI_3$	$CH_3NH_3PbI_3$
Crystal system	Cubic	Tetragonal	Orthorhombic
Measured energy gap (eV)		1.51	
Calculated energy gap (eV)	1.3	1.43	1.61

Table 5. Energy band gaps of $CH_3NH_3PbI_3$.

Atom	*x*	*y*	*z*	B (Å²)
Pb	0	0	0	1.13
Cl	0	0.0413	0.5	6.73
N	0.413	0.409	0.5	8.1
C	0.578	0.583	0.5	5.8

Table 6. Structural parameters of cubic $CH_3NH_3PbCl_3$. Space group *Pm3m* (Z=1), *a*=5.666 Å at 200 K. B is isotropic displacement parameter.

Structural parameters of cubic $CH_3NH_3PbCl_3$ and $CH_3NH_3PbBr_3$ are summarized as Table 6 and 7, respectively [14, 15]. They have similar structure parameters compared with the cubic

$CH_3NH_3PbI_3$, except for the lattice constants. Lattice parameters of these compounds are strongly depedent on the size of halogen ions, as shown in Figure 2. As summarized in Table 8, ion radii of halogen elements increase with increasing atomic numbers, which affect the lattice constants of $CH_3NH_3PbX_3$, as observed in Figure 2.

Atom	*x*	*y*	*z*	B (Å²)
Pb	0	0	0	1.61
Br	0	0.0413	0.5	5.41
N	0.413	0.417	0.5	6.02
C	0.578	0.582	0.5	6.05

Table 7. Structural parameters of cubic $CH_3NH_3PbBr_3$. Space group *Pm3m* (Z=1), *a*=5.933 nm at 298 K. B is isotropic displacement parameter.

Hologen element	F-	Cl^-	Br^-	I^-
Ion radius (Å)	1.33	1.81	1.96	2.20
14 group element		Ge^{2+}	Sn^{2+}	Pb^{2+}
Lattice parameters		0.73	0.93	1.18

Table 8. Ion radii of halogen and 14 group elements.

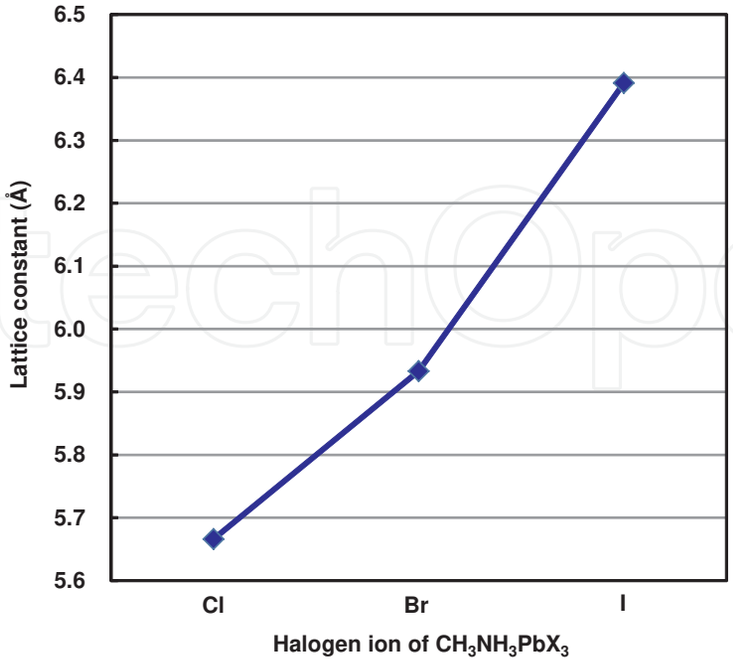

Figure 2. Lattice constants of $CH_3NH_3PbX_3$ (X=Cl, Br, or I).

http://dx.doi.org/10.5772/59284

4. X-ray diffraction of $CH_3NH_3PbI_3$

Microstructure of the perovskite phases can be investigated by X-ray diffraction (XRD). The XRD will indicate that the sample is a single phase or mixed phase. If the sample consists of nanoparticles or nanocrystals, the crystallite size can be estimated from the full width at half maximum (FWHM). From the XRD data, analyses of high-resolution TEM image and electron diffraction would become easier. If the sample is a known material, plane distances (*d*) and indices can be clarified from the diffraction peaks of XRD. When the sample has an unknown structure, the values of the plane distances can be obtained by the XRD, which will effectively stimulate the structure analysis.

Calculated X-ray diffraction patterns on the $CH_3NH_3PbI_3$ with cubic, tetragonal and orthorhombic structures is shown in Figure 3, and calculated X-ray diffraction parameters of cubic, tetragonal and orthorhombic $CH_3NH_3PbI_3$ are listed in Table 9, 10, and 11, respectively. For the cubic phase, site occupancies were set as 1/4 for I and 1/12 for C and N. Structure factors were averaged for each index. Site occupancies were set as 1/4 for C and N for the tetragonal $CH_3NH_3PbI_3$. Figure 4 is an enlarged calculated X-ray diffraction patterns of $CH_3NH_3PbI_3$. Reflection positions of 211 and 213 inconsistent with cubic symmetry for tetragonal structure are indicated by asterisks, which would be helpful for the distinction between the cubic and tetragonal phase [1].

Index	2θ (°)	*d-spacing (Å)*	|*F*|	Relative intensity (%)	Multiplicity
1 0 0	13.8449	6.3910	107.1	100	6
1 1 0	19.6279	4.5191	46.3	18	12
1 1 1	24.0990	3.6898	29.4	3	8
2 0 0	27.8973	3.1955	164.3	55	6
2 1 0	31.2695	2.8581	93.4	56	24
2 1 1	34.3423	2.6091	44.4	10	24
2 2 0	39.8633	2.2596	136.0	35	12
2 2 1	42.3942	2.1303	84.0	23	24
3 0 0	42.3942	2.1303	76.0	5	6
3 1 0	44.8082	2.0210	35.9	4	24
3 1 1	47.1237	1.9270	8.6	0.2	24
2 2 2	49.3555	1.8449	116.1	10	8
3 2 0	51.5149	1.7725	69.5	10	24
3 2 1	53.6114	1.7081	35.9	5	48
4 0 0	57.6458	1.5978	100.9	4	6
4 1 0	59.5956	1.5500	66.8	13	48

Table 9. Calculated X-ray diffraction parameters of cubic $CH_3NH_3PbI_3$. Equivlent indices were combined. Space group *Pm3m* (Z=1), *a*=6.391 Å at 330 K. *F* is structure factor.

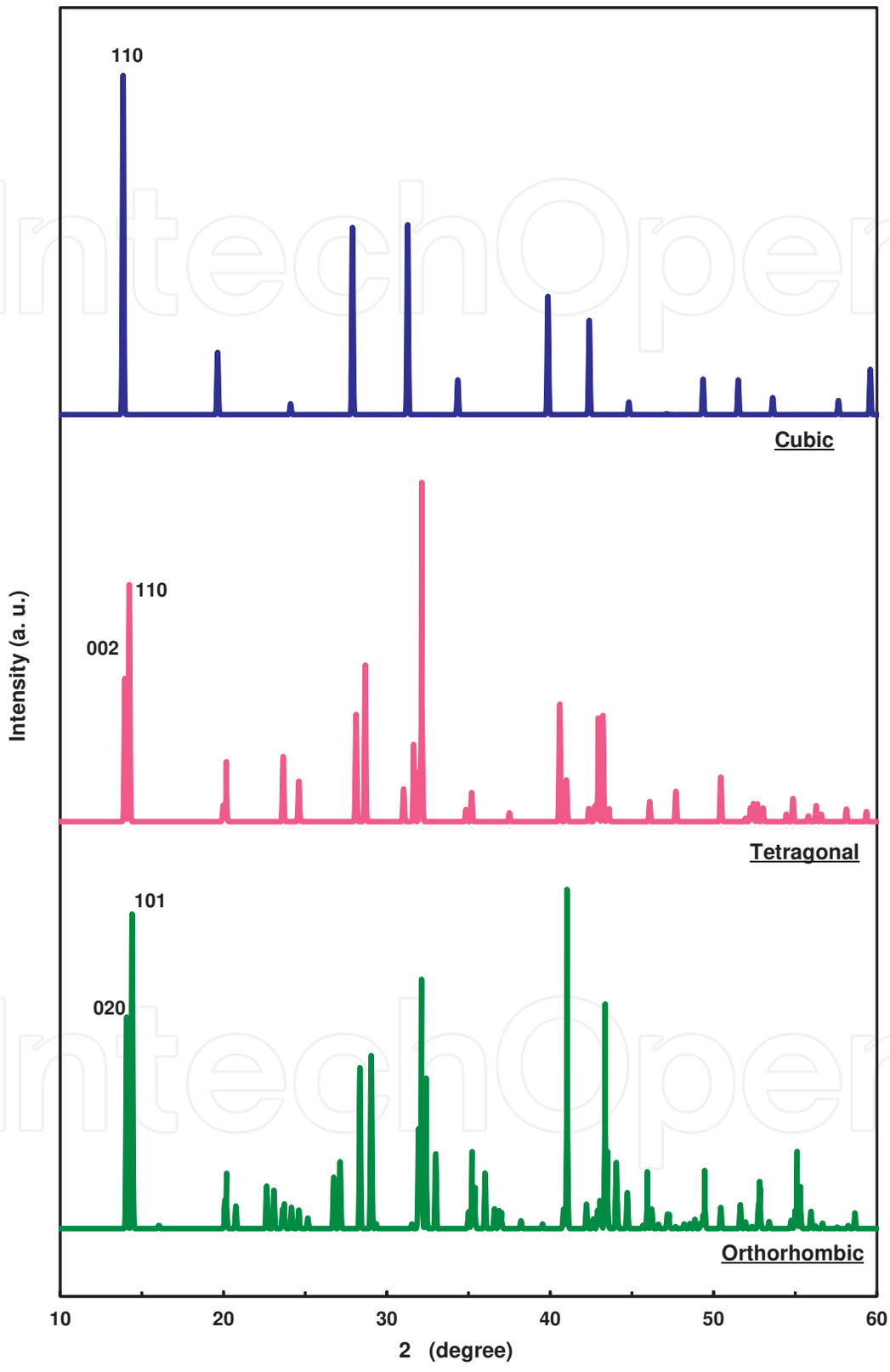

Figure 3. Calculated X-ray diffraction patterns of $CH_3NH_3PbI_3$ with cubic, tetragonal and orthorhombic structures.

http://dx.doi.org/10.5772/59284

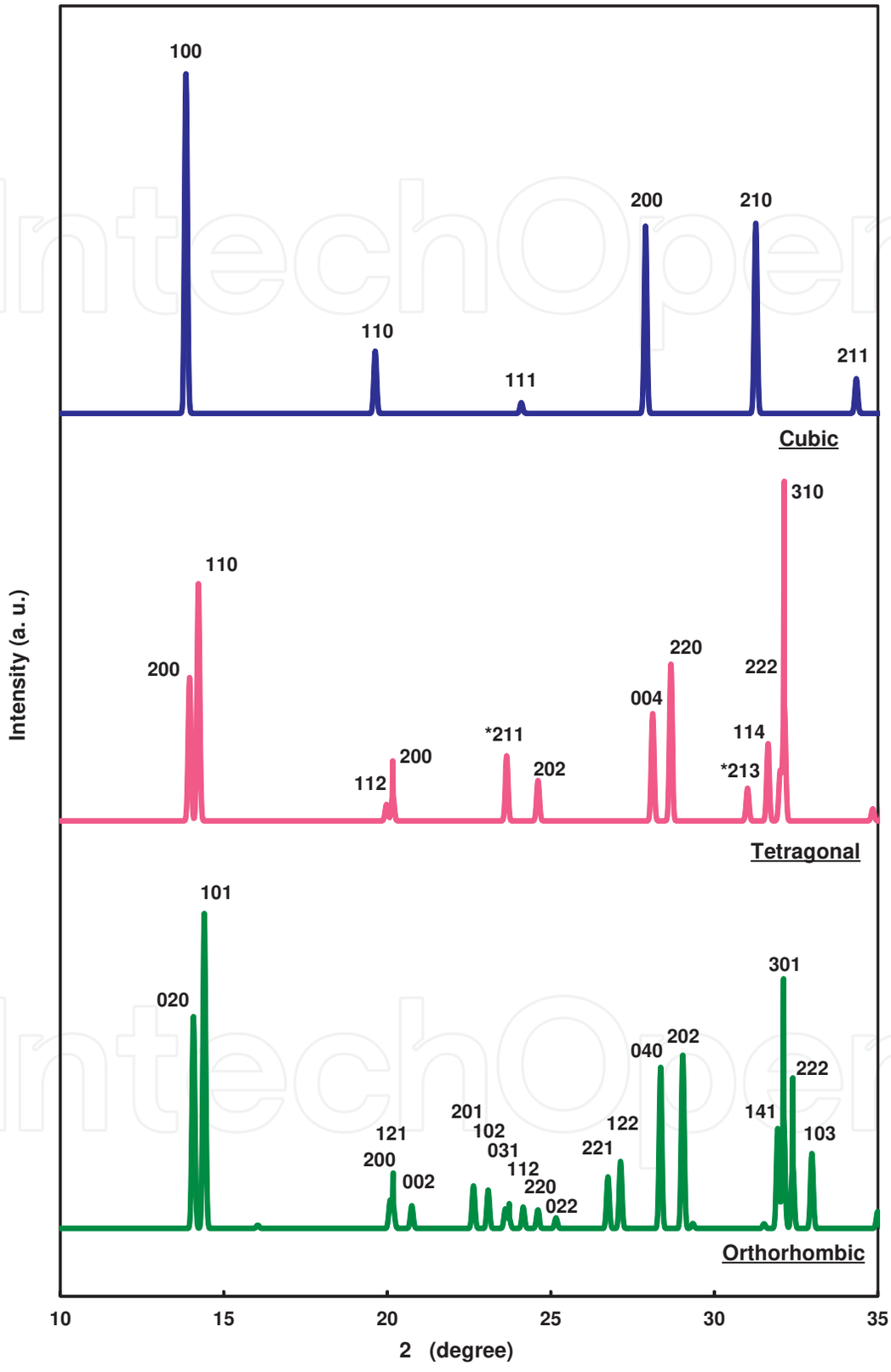

Figure 4. Enlarged calculated X-ray diffraction patterns of $CH_3NH_3PbI_3$ with cubic, tetragonal and orthorhombic structures. *Reflection positions inconsistent with cubic symmetry for tetragonal structure.

Index	2θ (°)	*d-spacing (Å)*	$\|F\|$	Relative intensity (%)	Multiplicity
0 0 2	13.9513	6.3425	477.0	60	2
1 1 0	14.2216	6.2225	442.5	100	4
1 1 2	19.9730	4.4418	116.8	7	8
2 0 0	20.1647	4.4000	211.6	11	4
2 1 1	23.6509	3.7587	195.7	27	16
2 0 2	24.6041	3.6152	227.6	17	8
0 0 4	28.1149	3.1713	852.4	45	2
2 2 0	28.6684	3.1113	744.0	66	4
2 1 3	31.0176	2.8808	184.5	14	16
1 1 4	31.6405	2.8255	410.3	33	8
2 2 2	32.0148	2.7933	331.7	21	8
3 1 0	32.1387	2.7828	511.0	49	8
2 0 4	34.8441	2.5727	180.5	5	8
3 1 2	35.1881	2.5483	199.6	12	16
3 2 1	37.4940	2.3967	117.9	4	16
2 2 4	40.5874	2.2209	665.6	50	8
4 0 0	40.9903	2.2000	566.6	18	4
2 1 5	42.3526	2.1323	165.5	6	16
0 0 6	42.7343	2.1142	415.0	4	2
3 2 3	42.7418	2.1138	109.2	2	16
4 1 1	42.9354	2.1047	277.8	15	16
3 1 4	43.2169	2.0917	479.9	45	16
4 0 2	43.5043	2.0785	222.4	5	8
3 3 0	43.5998	2.0742	225.3	2	4
4 2 0	46.0901	1.9677	317.2	8	8
2 0 6	47.6844	1.9056	155.2	2	8
4 1 3	47.6913	1.9053	265.2	11	16
4 0 4	50.4445	1.8076	523.0	19	8
3 2 5	51.9446	1.7589	106.0	1	16
2 2 6	52.2716	1.7487	303.6	6	8
4 3 1	52.4442	1.7433	171.5	4	16
3 3 4	52.6864	1.7359	218.2	3	8
5 1 0	53.0165	1.7258	307.9	6	8
3 1 6	54.4599	1.6834	165.0	3	16
4 2 4	54.8632	1.6720	294.6	10	16
2 1 7	55.8045	1.6460	149.8	2	16

4 1 5	56.2804	1.6332	250.9	7	16
4 3 3	56.5963	1.6249	171.4	3	16
0 0 8	58.1285	1.5856	657.6	5	2
4 4 0	59.3600	1.5556	423.9	4	4
1 1 8	60.1739	1.5365	353.3	6	8

Table 10. Calculated X-ray diffraction parameters of tetragonal $CH_3NH_3PbI_3$. Space group *I4/mcm* (Z=4), *a*=8.800 Å, c=12.685 Å at 220 K.

Index	2θ (°)	*d-spacing (Å)*	|*F*|	Relative intensity (%)	Multiplicity
0 2 0	14.0679	6.2902	462.7	67	2
1 0 1	14.3989	6.1463	408.5	100	4
1 1 1	16.0356	5.5225	32.8	1	8
2 0 0	20.0813	4.4181	238.7	9	2
1 2 1	20.1828	4.3961	106.9	7	8
0 0 2	20.7483	4.2775	225.2	7	2
2 0 1	22.6324	3.9255	239.3	14	4
1 0 2	23.0816	3.8501	231.4	12	4
0 3 1	23.6082	3.7654	168.3	6	4
2 1 1	23.7239	3.7473	86.8	3	8
1 1 2	24.1539	3.6816	128.7	7	8
2 2 0	24.6029	3.6154	172.8	6	4
0 2 2	25.1559	3.5372	132.9	3	4
2 2 1	26.7471	3.3302	221.7	16	8
1 2 2	27.1323	3.2838	256.6	21	8
0 4 0	28.3536	3.1451	834.3	51	2
2 0 2	29.0316	3.0732	627.4	55	4
2 3 0	29.3402	3.0415	108.2	2	4
1 3 2	31.5191	2.8361	80.9	2	8
1 4 1	31.9379	2.7998	373.2	32	8
3 0 1	32.1130	2.7850	560.5	35	4
0 1 3	32.1584	2.7811	155.6	3	4
2 2 2	32.3965	2.7612	304.2	20	8
1 0 3	32.9780	2.7139	473.6	24	4
2 4 0	34.9912	2.5622	239.4	5	4

3 2 1	35.2135	2.5465	244.8	11	8
0 4 2	35.3949	2.5339	225.2	5	4
1 2 3	36.0126	2.4918	317.4	18	8
2 4 1	36.5799	2.4545	193.6	6	8
1 4 2	36.8717	2.4357	185.8	6	8
3 0 2	37.0262	2.4259	145.8	2	4
2 1 3	38.2065	2.3536	127.4	3	8
1 3 3	39.5204	2.2784	101.4	1	8
4 0 0	40.8148	2.2091	432.0	6	2
2 4 2	41.0283	2.1980	555.9	41	8
4 0 1	42.2164	2.1389	281.7	5	4
0 0 4	42.2189	2.1388	305.7	3	2
2 5 1	42.6467	2.1183	161.0	3	8
1 5 2	42.9036	2.1062	142.9	2	8
3 3 2	43.0398	2.0999	157.9	3	8
0 6 0	43.1073	2.0967	330.6	3	2
3 4 1	43.3616	2.085	506.1	30	8
4 2 0	43.3783	2.0843	145.8	1	4
2 3 3	43.4643	2.0803	157.5	3	8
1 0 4	43.4991	2.0787	318.3	6	4
1 4 3	44.0352	2.0547	429.7	21	8
1 1 4	44.1197	2.0509	140.7	2	8
4 2 1	44.7146	2.0250	292.5	9	8
0 2 4	44.7169	2.0249	202.1	2	4
1 6 1	45.6801	1.9844	100.8	1	8
1 2 4	45.9414	1.9738	258.0	7	8
4 0 2	46.2136	1.9628	352.1	6	4
3 2 3	46.5832	1.9481	73.0	1	8
2 5 2	46.6144	1.9468	93.9	1	8
2 0 4	47.1728	1.9251	308.8	5	4
3 4 2	47.2817	1.9209	124.0	1	8
0 5 3	48.1925	1.8867	181.8	2	4
4 2 2	48.5489	1.8737	135.7	2	8
1 3 4	48.8598	1.8625	183.1	3	8

2 6 1	49.2266	1.8494	148.3	2	8
1 5 3	49.3503	1.8451	124.9	1	8
1 6 2	49.4567	1.8414	175.3	3	8
2 2 4	49.4736	1.8408	218.7	4	8
4 4 0	50.442	1.8077	403.4	7	4
4 4 1	51.6367	1.7686	236.3	4	8
0 4 4	51.6388	1.7686	287.3	3	4
0 7 1	51.9470	1.7588	234.2	2	4
4 0 3	52.3451	1.7464	135.0	1	4
2 5 3	52.7109	1.7351	82.5	1	8
1 4 4	52.7410	1.7342	270.6	5	8
2 6 2	52.8123	1.7320	242.3	4	8
5 0 1	52.8555	1.7307	280.3	3	4
4 1 3	52.8858	1.7298	121.2	1	8
3 1 4	53.3946	1.7145	162.9	2	8
3 6 1	54.7548	1.6751	197.8	3	8
3 2 4	54.9839	1.6686	176.9	2	8
4 4 2	55.1098	1.6651	333.9	8	8
2 7 0	55.1235	1.6647	160.7	1	4
4 5 0	55.2931	1.6600	194.8	1	4
1 6 3	55.3226	1.6592	258.8	4	8
2 4 4	55.9564	1.6419	290.5	5	8
1 2 5	56.6693	1.6229	166.9	2	8
2 1 5	58.2395	1.5829	131.8	1	8
0 8 0	58.6587	1.5726	586.0	5	2
4 0 4	60.1713	1.5366	266.9	2	4

Table 11. Calculated X-ray diffraction parameters of orthorhombic $CH_3NH_3PbI_3$. Space group *Pnma* (*Z*=4), *a*=8.8362 Å, *b*=12.5804 Å, *c*=8.5551 Å at 100 K. B is isotropic displacement parameter. All occupancy factors 1.0.

Calculated X-ray diffraction patterns of $CH_3NH_3PbI_3$ with various FWHM values are shown in Figure 5. When the crystallite sizes decrease, the FWHM values increase, and different peak intensities are observed in Figure 5.

Figure 6 is an enlarged calculated X-ray diffraction patterns of $CH_3NH_3PbI_3$. With increasing FWHM values, the diffraction peaks of 200 and 110 seem to be combined, which should be very careful for the XRD structure analysis.

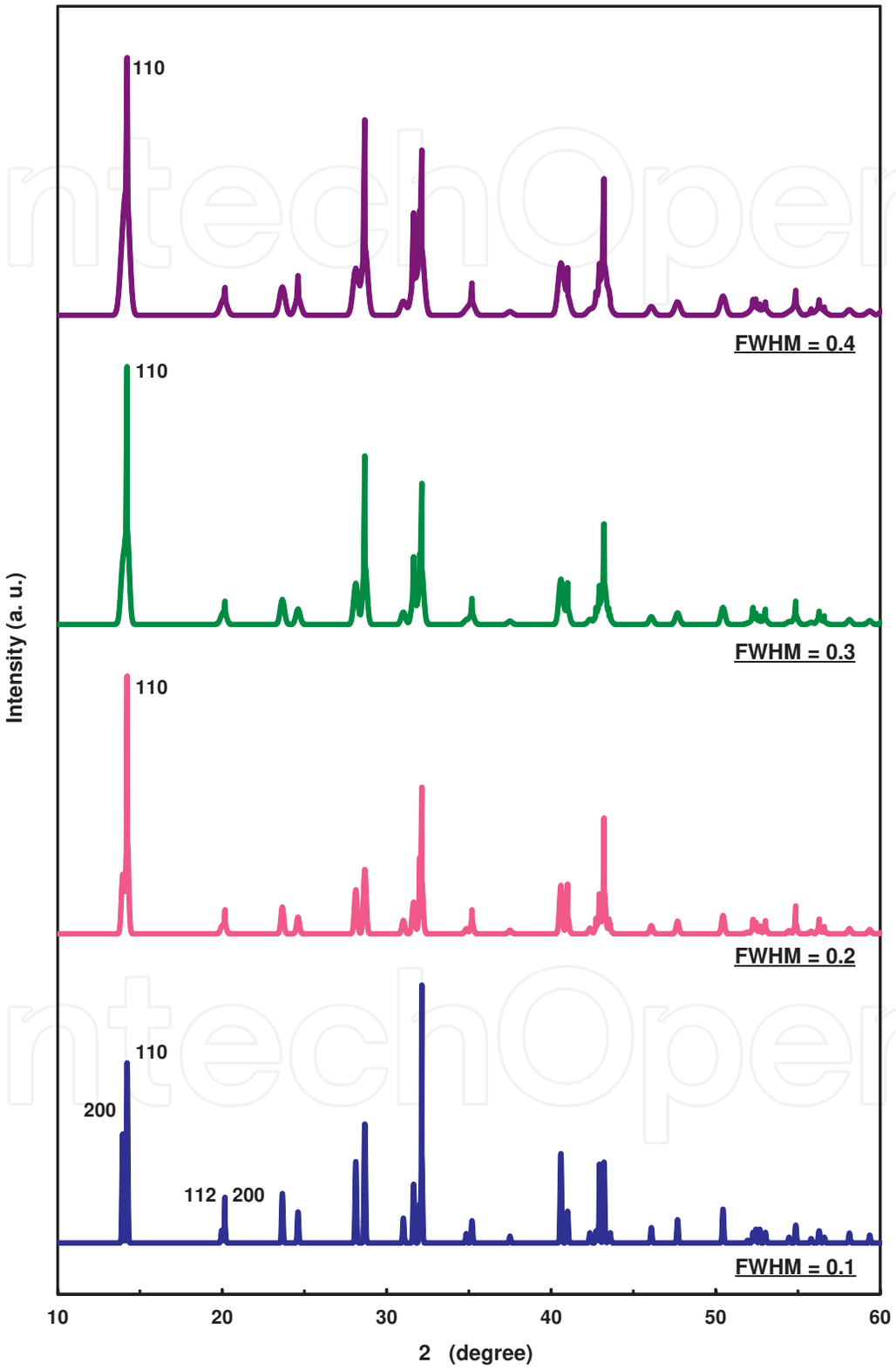

Figure 5. Calculated X-ray diffraction patterns of $CH_3NH_3PbI_3$ with various FWHM values.

http://dx.doi.org/10.5772/59284

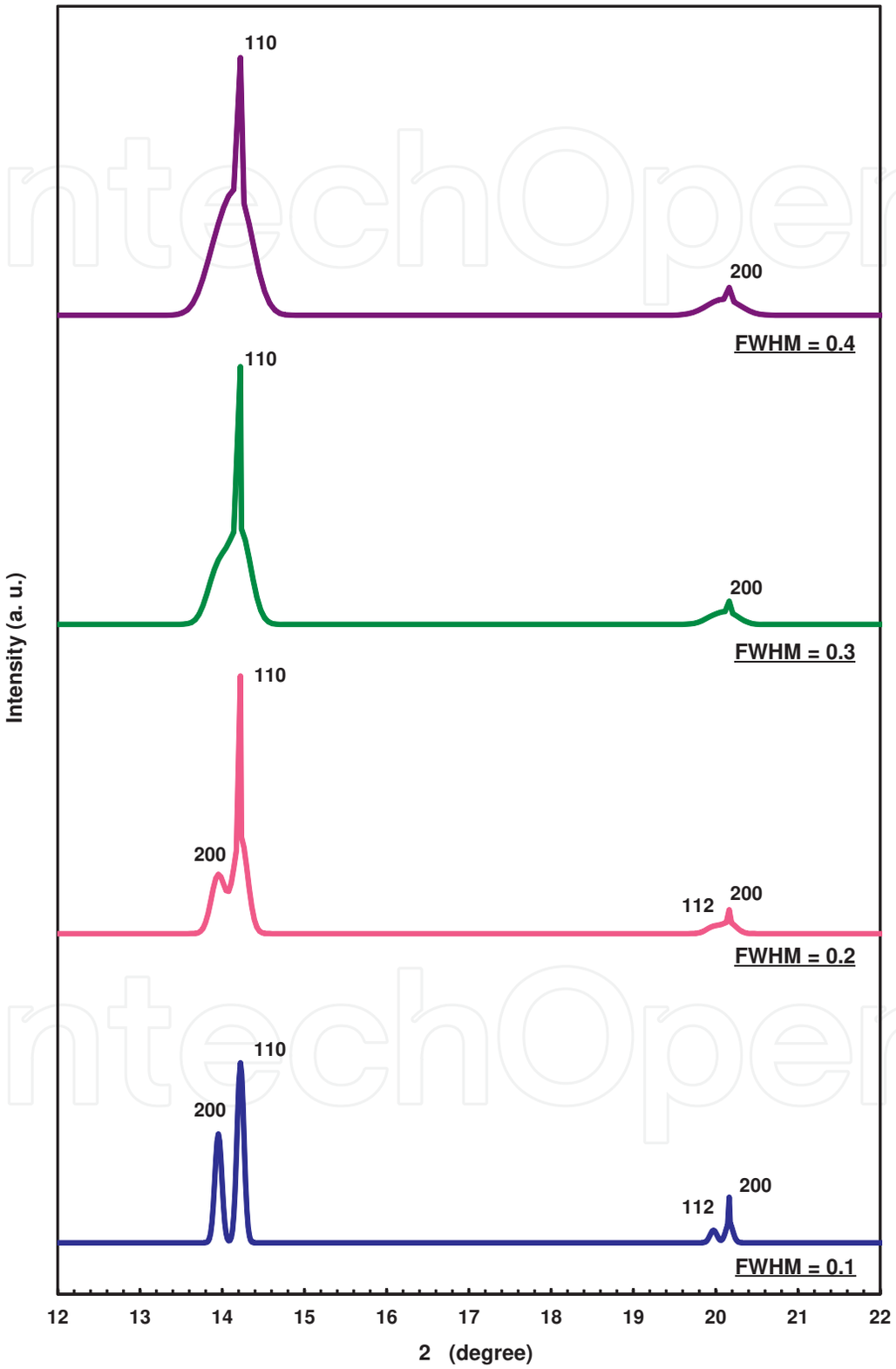

Figure 6. Enlarged calculated X-ray diffraction patterns of $CH_3NH_3PbI_3$ with various FWHM values.

5. Electron diffraction of $CH_3NH_3PbI_3$

When the sample amount, sample area or film thickness is smaller, it is difficult to obtain the necessary diffraction amplitude by XRD. Since the amount is enough for the TEM observation, only TEM observation may be applied to obtain the structure data. To obtain the information on the fundamental atomic arrangements, electron diffraction patterns should be taken along the various directions of the crystal, and the fundamental crystal system and lattice constants may be estimated. Then, high-resolution TEM observation and composition analysis by energy dispersive X-ray spectroscopy are performed, and the approximate atomic structure model is constructed. Most of the materials have similar structures to the known materials, and the structures will be estimated if the database on the known structures is available. For example, lots of new structures were found for high-Tc superconducting oxides, which have basic perovskite structures, and the approximate atomic structure models can be constructed from the high-resolution TEM images, electron diffraction patterns, and composition analysis of the elements [17, 19].

If a structure of the TEM specimen is known, observation direction of the crystal should be selected, and electron diffraction pattern along the direction should be estimated. Any regions selected by the selected area aperture can be observed in electron diffraction patterns, and the structure can be easily analyzed by comparing TEM images with electron diffraction patterns. When electron diffraction pattern is observed in the selected area, the diffraction pattern is often inclined from the aimed direction, which is noticed from the asymmetry of the electron diffraction pattern. The sample holder can be usually tilted along two directions, and the specimen should be tilted as the diffraction pattern shows center symmetry. Atomic structure models of cubic $CH_3NH_3PbI_3$ observed along varioius directions are shown in Figure 7. Note that the atomic positions of CH_3, NH_3 and I are disordered as observed in the structure models. Corresponding electron diffraction patterns of cubic $CH_3NH_3PbI_3$ calculated along the [100], [110], [111] and [210] directions are shown in Figure 8.

Atomic structure models of tetragonal $CH_3NH_3PbI_3$ observed along [001], [100], [021], [221] and [110] are shown in Figure 9, which correspond to [001], [110], [111], [210] and [100] of cubic phase in Figure 8, respectively. Atomic positions of I are fixed for the tetragonal phase, and only atomic positions of CH_3 and NH_3 are disordered. For the tetragonal phase, the crystal symmetries are lowered as indicated by arrows in Figure 9(c) and 9(e). Several diffraction spots in Figure 9 have different diffraction intensities compared with Figure 8, which would be due to the different crystal symmetry of the $CH_3NH_3PbI_3$ compound.

High-resolution TEM observations have been performed for the perovskite materials [20], and the nanostructures were discussed. Although TEM is a powerful tool for nanostructured materials, sample damage by electron beam irradiation should be avoided, because the $CH_3NH_3PbI_3$ are known to be unstable during annealing at elevated temperatures. Several TEM results have been reported for the $CH_3NH_3PbI_3$ and $CH_3CH_2NH_3PbI_3$, and the structures were discussed by electron diffraction and high-resolution images in these works [1, 9, 28].

http://dx.doi.org/10.5772/59284

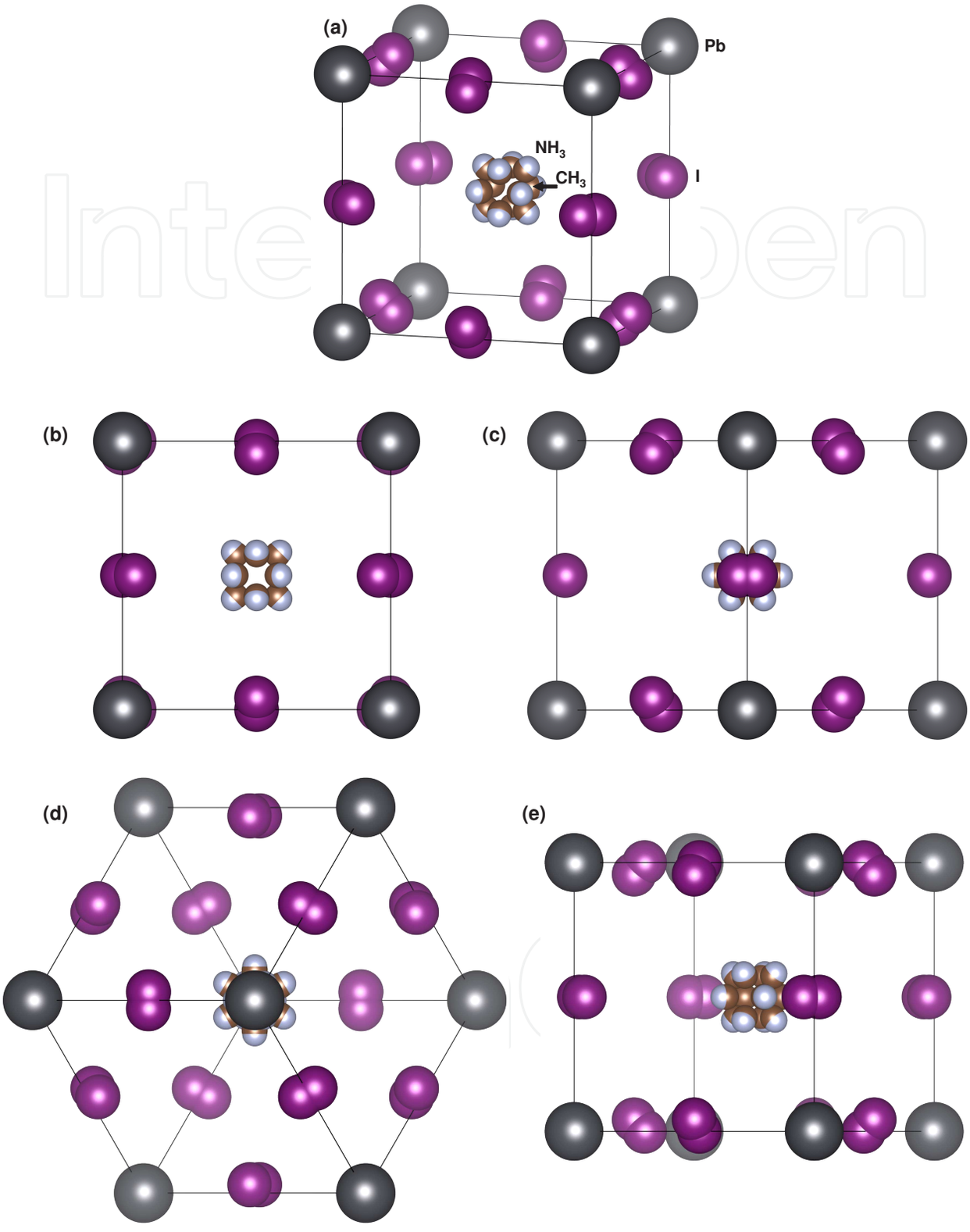

Figure 7. Atomic structure models of cubic $CH_3NH_3PbI_3$ observed along (a) perspevtive view, (b) [100], (c) [110], (d) [111] and (e) [210].

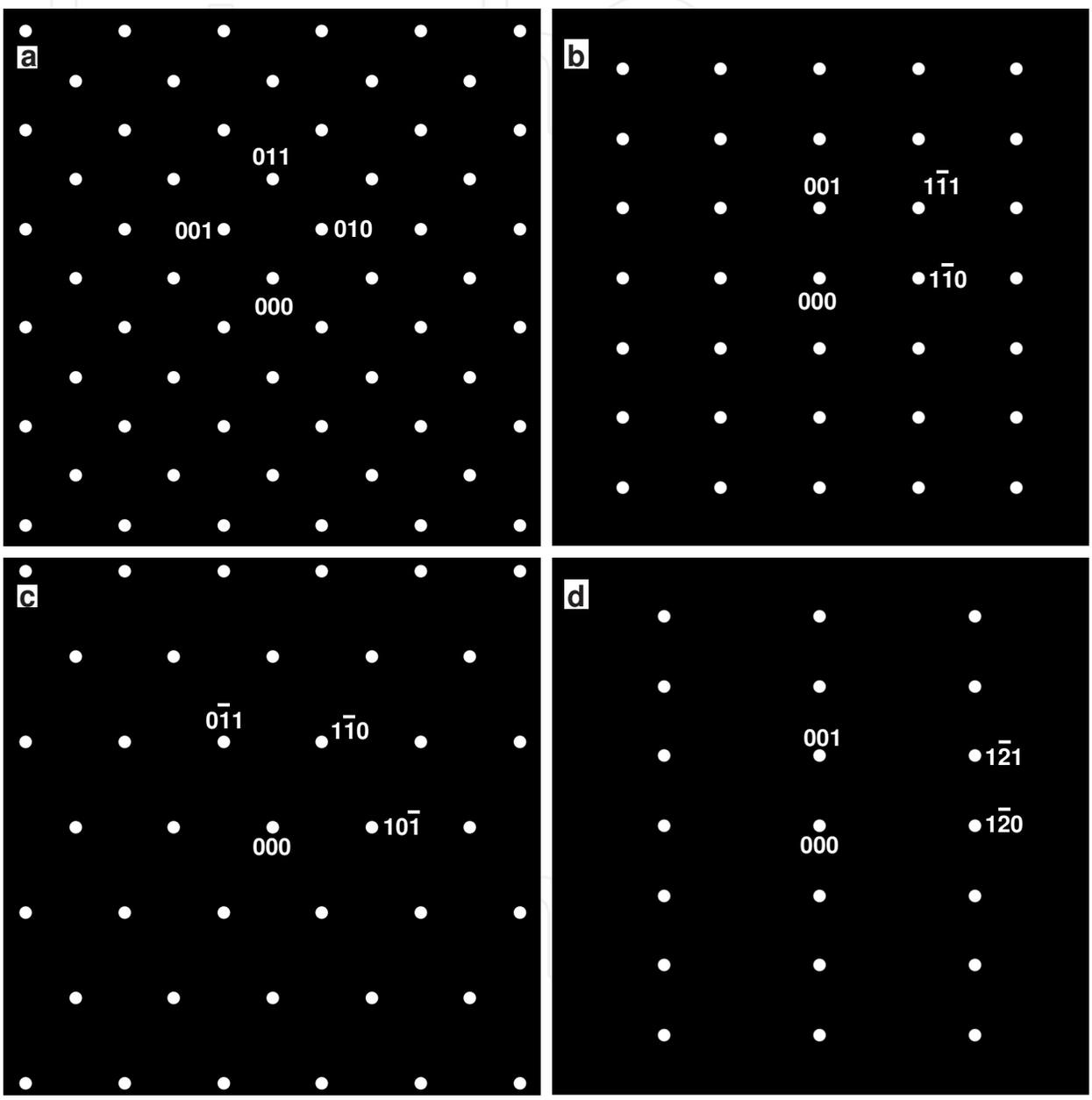

Figure 8. Calculated electron diffraction patterns of cubic $CH_3NH_3PbI_3$ along (a) [100], (b) [110], (c) [111] and (d) [210].

http://dx.doi.org/10.5772/59284

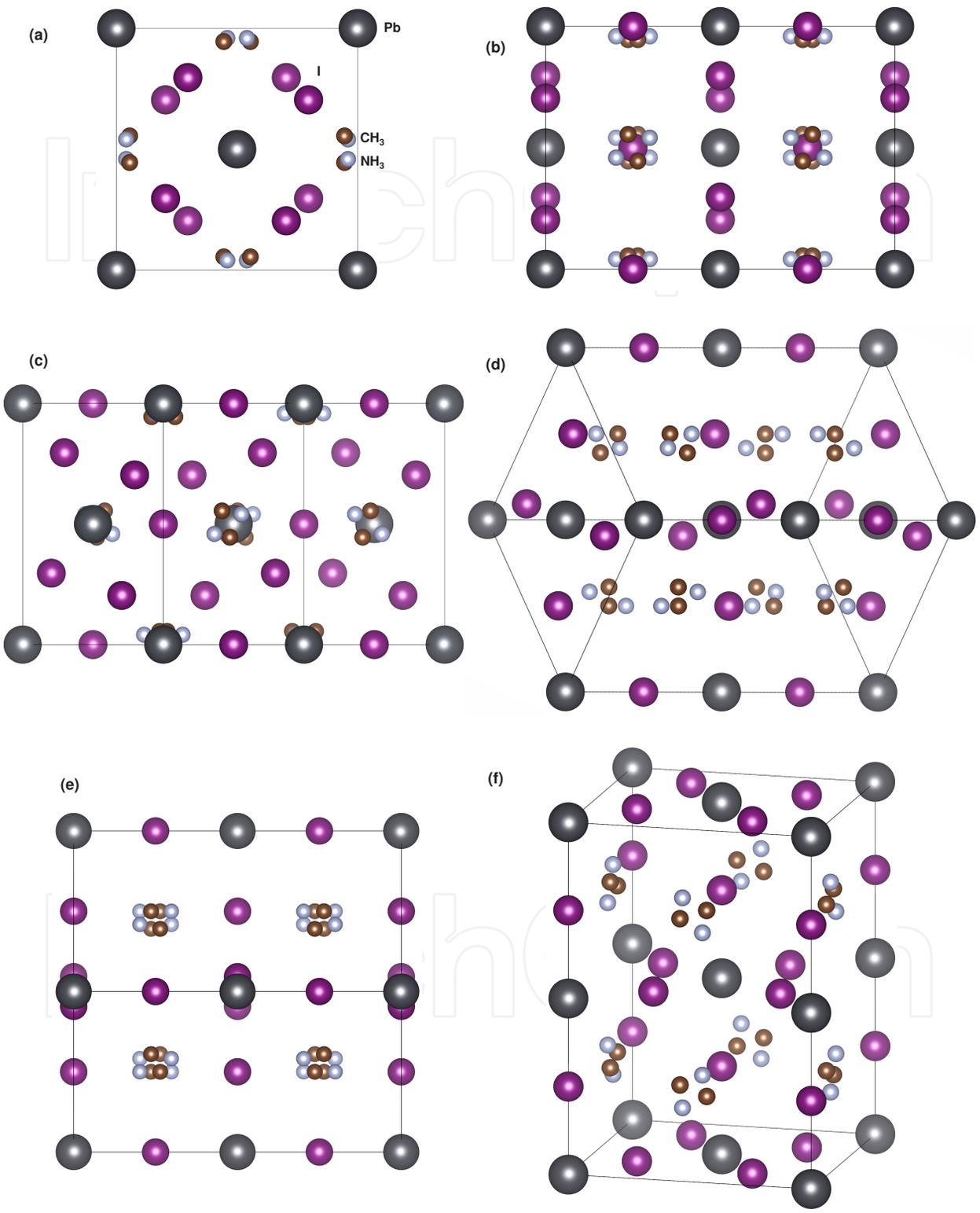

Figure 9. Atomic structure models of tetragonal $CH_3NH_3PbI_3$ observed along (a) [001], (b) [100], (c) [021], (d) [221] and (e) [110] and (f) perspevtive view.

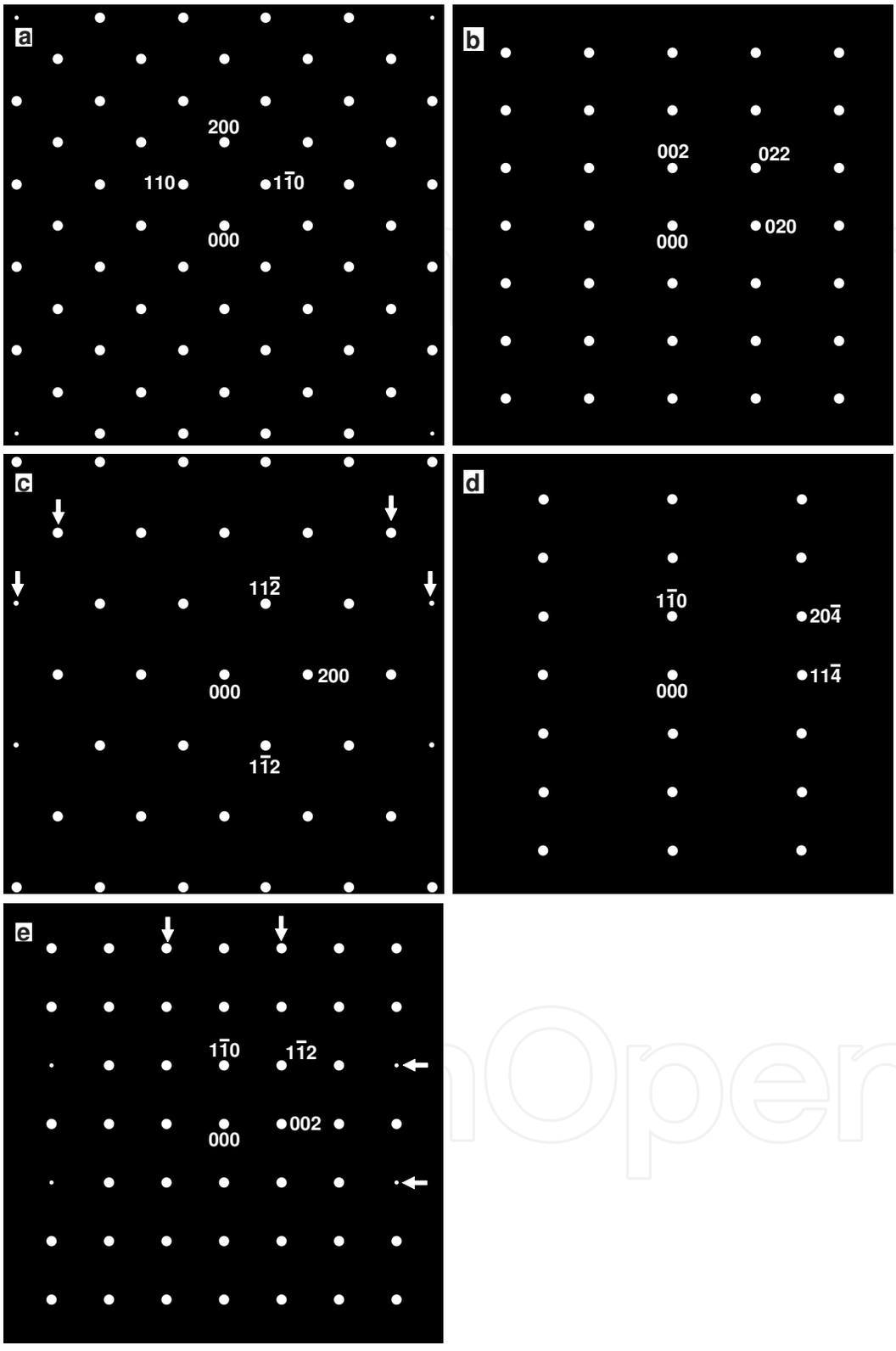

Figure 10. Calculated electron diffraction patterns of tetragonal $CH_3NH_3PbI_3$ along (a) [001], (b) [100], (c) [021], (d) [221] and (e) [110].

http://dx.doi.org/10.5772/59284

6. Other compounds with perovskite structures for solar cells

In addition to $CH_3NH_3PbX_3$ (X=Cl, Br, or I) compounds, various perovskite compounds with perovskite structures for solar cells have benn reported and summarized [1]. Crystal systems and temperatures of $CsSnI_3$ are listed in Table 12, which has very similar structures and phase transitions [3] compared with the $CH_3NH_3PbX_3$. Solar cells with F-doped $CsSnI_{2.95}F_{0.05}$ provided an photo-conversion efficiency of 8.5% [4].

Temperature (K)	300	350	478
Crystal system	Orthorhombic	Tetragonal	Cubic
Space group	*Pnma*	*P4/mbm*	*Pmm*
Z	4	2	1
Lattice parameters	*a* = 8.6885 Å *b* = 12.3775 Å *c* = 8.3684 Å	*a* = 8.7182 Å *c* = 6.1908 Å	*a* = 6.1057 Å

Table 12. Crystal systems and temperatures of $CsSnI_3$.

Temperature (K)	2	250	370	475
Crystal system	Monoclinic	Orthorhombic	Trigonal	Cubic
Space group	$P2_1/n$	*Pnma*	*R3m*	*Pmm*
Z	4	4	1	1
Lattice parameters	*a* = 10.9973 Å *b* = 7.2043 Å *c* = 8.2911 Å α = 90.470°	*a* = 11.1567 Å *b* = 7.3601 Å *c* = 8.2936 Å	*a* = 5.6784 Å α = 90.945°	*a* = 5.6917 Å

Table 13. Crystal systems and temperatures of $CH_3NH_3GeCl_3$.

Similar structures of $CH_3NH_3GeCl_3$ and $CH_3NH_3SnCl_3$ are shown in Table 13 and 14, respectively [28, 26]. Ion radii of Ge and Sn ions are listed in Table 8, and they can be substituted for the Pb atoms in $CH_3NH_3PbX_3$. Lead-free $CH_3NH_3SnI_3$ solar cells were developed, which provided 5.7% efficiency [7]. $(CH_3CH_2NH_3)PbI_3$ with a 2H perovskite structure was reported, which privided 2.4% efficiency [9]. Perovskite oxides such as $[KNbO_3]_{0.9}[BaNi_{0.5}Nb_{0.5}O_{3-x}]_{0.1}$ were found to have an energy gap of ~1.4 eV, which would also be expected as solar cell materials [5].

Temperature (K)	297	318	350	478
Crystal system	Triclinic	Monoclinic	Trigonal	Cubic
Space group	*P*1	*Pc*	*R3m*	*Pmm*
Z	4	4	1	1
Lattice parameters	a = 5.726 Å b = 8.227 Å c = 7.910 Å α = 90.40° β = 93.08° γ = 90.15°	a = 5.718 Å b = 8.236 Å c = 7.938 Å β = 93.08°	a = 5.734 Å α = 91.90°	a = 5.760 Å

Table 14. Crystal systems and temperatures of $CH_3NH_3SnCl_3$.

7. Conclusion

Crystal structures of perovskite-type $CH_3NH_3PbI_3$ compounds with cubic, tetragonal and orthorhombic structures were reviewed and summarized, and X-ray diffraction parameters and diffraction patterns were calculated and presented. Electron diffraction patterns were also calculated along various crystal directions and discussed. Other perovskite compounds such as $CH_3NH_3PbCl_3$, $CH_3NH_3PbBr_3$, $CH_3NH_3GeCl_3$, $CH_3NH_3SnCl_3$, and $CsSnI_3$ were also reviewed, which are expected as next generation, organic-inorganic hybrid solar cells with high photo-conversion efficiencies.

Acknowledgements

The author would like to acknowledge M. Zushi and A. Suzuki for fruitful discussion on the perovskite materials for solar cells.

Author details

Takeo Oku*

Address all correspondence to: oku@mat.usp.ac.jp

The University of Shiga Prefecture, Japan

References

[1] Baikie, T.; Fang, Y,; Kadro, J. M.; Schreyer, M.; Wei, F.; Mhaisalkar, S. G.; Grätzel, M. & Whitec, T. J. (2013). Synthesis and crystal chemistry of the hybrid perovskite (CH_3NH_3)PbI3 for solid–state sensitised solar cell applications, *Journal of Materials Chemistry A*, Vol. 1, pp. 5628–5641.

[2] Burschka, J.; Pellet, N.; Moon, S.–J.; Humphry–Baker, R.; Gao, P.; Nazeeruddin, M. K. & Grätzel, M. (2013). Sequential deposition as a route to high–performance perovskite–sensitized solar cells. *Nature*, Vol. 499, pp. 316–320.

[3] Chung, I.; Song, J. H.; Im, J.; Androulakis, J.; Malliakas, C. D.; Li, H.; Freeman, A. J.; Kenney, J. T. & Kanatzidis, M. G. (2012A). CsSnI3: semiconductor or metal? High electrical conductivity and strong near–infrared photoluminescence from a single material. High hole mobility and phase–transitions. *Journal of the American Chemical Society*, Vol. 134, pp. 8579–8587.

[4] Chung, I.; Lee, B.; He, J.; Chang, R. P. H. & Kanatzidis, M. G. (2012B). All–solid–state dye–sensitized solar cells with high efficiency. *Nature*, Vol. 485, pp. 486–489.

[5] Grinberg, I.; West, D. V.; Torres, M.; Gou, G.; Stein, D. M.; Wu, L.; Chen, G.; Gallo, E. M.; Akbashev, A. R.; Davies, P. K.; Spanier J. E. & Rappe A. M. (2013). Perovskite oxides for visible–light–absorbing ferroelectric and photovoltaic materials. *Nature*, Vol. 503, pp. 509–512.

[6] Hahn, T. (1995). *International tables for crystallography, Volume A*. Kluwer Academic Publishers, The Netherland.

[7] Hao, F.; Stoumpos, C. C.; Cao, D. H.; Chang, R. P. H. & Kanatzidis M. G. (2014). Lead–free solid–state organic–inorganic halide perovskite solar cells. *Nature Photonics*, Vol. 8, pp. 489–494.

[8] Im, J.–H.; Lee, C.–R.; Lee, J.–W.; Park, S.–W. & Park, N.–G. (2011). 6.5% efficient perovskite quantum–dot–sensitized solar cell. *Nanoscale*, Vol. 3, pp. 4088–4093.

[9] Im, J.–H.; Chung, J.; Kim S.–J. & Park N.–G. (2012). Synthesis, structure, and photovoltaic property of a nanocrystalline 2H perovskite–type novel sensitizer ($CH_3CH_2NH_3$)PbI3. *Nanoscale Research Letters*, Vol. 7, 353–1–7.

[10] Kawamura, Y.; Mashiyama, H. & Hasebe, K. (2002). Structural study on cubic–tetragonal transition of CH3NH3PbI3. *Journal of the Physical Society of Japan*, Vol. 71, pp. 1694–1697.

[11] Kojima, A.; Teshima, K.; Shirai, Y. & Miyasaka T. (2009). Organometal halide perovskites as visible–light sensitizers for photovoltaic cells. *Journal of the American Chemical Society*, Vol. 131, pp. 6050–6051.

[12] Lee, M. M.; Teuscher, J.; Miyasaka, T.; Murakami, T. N. & Snaith, H. J. (2012). Efficient hybrid solar cells based on meso–superstructured organometal halide perovskites. *Science*, Vol. 338, pp. 643–647.

[13] Liu, D. & Kelly, T. L. (2014). Perovskite solar cells with a planar heterojunction structure prepared using room–temperature solution processing techniques. *Nature Photonics*, Vol. 8, pp. 133–138.

[14] Mashiyama, H.; Kurihara, Y. & Azetsu T. (1998). Disordered cubic perovskite structure of CH3NH3PbX3 (X=Cl, Br, I). *Journal of the Korean Physical Society*, Vol. 32, pp. S156–S158.

[15] Mashiyama, H.; Kawamura, Y.; Magome, E. & Kubota Y. (2003). Displacive character of the cubic–tetragonal transition in $CH_3NH_3PbX_3$. *Journal of the Korean Physical Society*, Vol. 42, pp. S1026–S1029.

[16] Oku, T.; Kakuta, N.; Kobayashi, K.; Suzuki, A. & Kikuchi, K. (2011). Fabrication and characterization of TiO2–based dye–sensitized solar cells. *Progress in Natural Science: Materials International*, Vol. 21, pp. 122–126.

[17] Oku, T. (2012). Direct structure analysis of advanced nanomaterials by high–resolution electron microscopy. *Nanotechnology Reviews*, Vol. 1, pp. 389–425.

[18] Oku, T.; Takeda, A.; Nagata, A.; Kidowaki, H.; Kumada, K.; Fujimoto, K.; Suzuki, A.; Akiyama, T.; Yamasaki, Y. & Ōsawa, E. (2013). Microstructures and photovoltaic properties of C60 based solar cells with copper oxides, CuInS2, phthalocyanines, porphyrin, PVK, nanodiamond, germanium and exciton diffusion blocking layers. *Materials Technology*, Vol. 28, pp. 21–39.

[19] Oku, T. (2014). Structure analysis of advanced nanomaterials: nanoworld by high–resolution electron microscopy. Walter De Gruyter Inc. Germany.

[20] Oku, T. (2014). High–resolution electron microscopy and electron diffraction of perovskite–type superconducting copper oxides. *Nanotechnology Reviews*, Vol. 3, 413–444.

[21] Onoda–Yamamuro, N.; Matsuo, T. & Suga, H. (1990). Calorimetric and IR spectroscopic studies of phase transitions in methylammonium trihalogenoplumbates (II). *Journal of Physics and Chemistry of Solids*, Vol. 51, pp. 1383–1395.

[22] Poglitsch, A. & Weber, D. (1987). Dynamic disorder in methylammonium trihalogenoplumbates (II) observed by millimeter–wave spectroscopy. *The Journal of Chemical Physics*, Vol. 87, pp. 6373–6378.

[23] Wang, J. T.–W.; Ball, J. M.; Barea, E. M.; Abate, A.; Alexander–Webber, J. A.; Huang, J.; Saliba, M.; Mora–Sero, I.; Bisquert, J.; Snaith, H. J. & Nicholas, R. J. (2014). Low–temperature processed electron collection layers of graphene/TiO2 nanocomposites in thin film perovskite solar cells. *Nano Letters*, Vol. 14, pp. 724–730.

[24] Weber, D. (1978). $CH_3NH_3PbX_3$, ein Pb(II)–system mit kubischer perowskitstruktur *Zeitschrift für Naturforschung B*, Vol. 33, pp. 1443–1445.

[25] Yamada, K.; Kuranaga, Y.; Ueda, K.; Goto, S.; Okuda, T. & Furukawa, Y. (1998). Phase transition and electric conductivity of ASnCl3 (A = Cs and CH3NH3). *Bulletin of the Chemical Society of Japan*, Vol. 71, pp. 127–134.

[26] Yamada, K.; Mikawa, K.; Okuda, T. & Knight, K. S. (2002) Static and dynamic structures of CD3ND3GeCl3 studied by TOF high resolution neutron powder diffraction and solid state NMR. *Journal of the Chemical Society, Dalton Transactions*, pp. 2112–2118.

[27] Zhou, H.; Chen, Q.; Li, G.; Luo, S.; Song, T.–B.; Duan, H.–S.; Hong, Z.; You, J.; Liu, Y. & Yang, Y. (2014). Interface engineering of highly efficient perovskite solar cells. *Science*, Vol. 345, pp. 542–546.

[28] Zushi, M.; Suzuki, A.; Akiyama, T. & Oku T. (2014). Fabrication and characterization of $TiO_2/CH_3NH_3PbI_3$–based photovoltaic devices. Chemistry Letters, Vol. 43, pp. 916–918.

IntechOpen